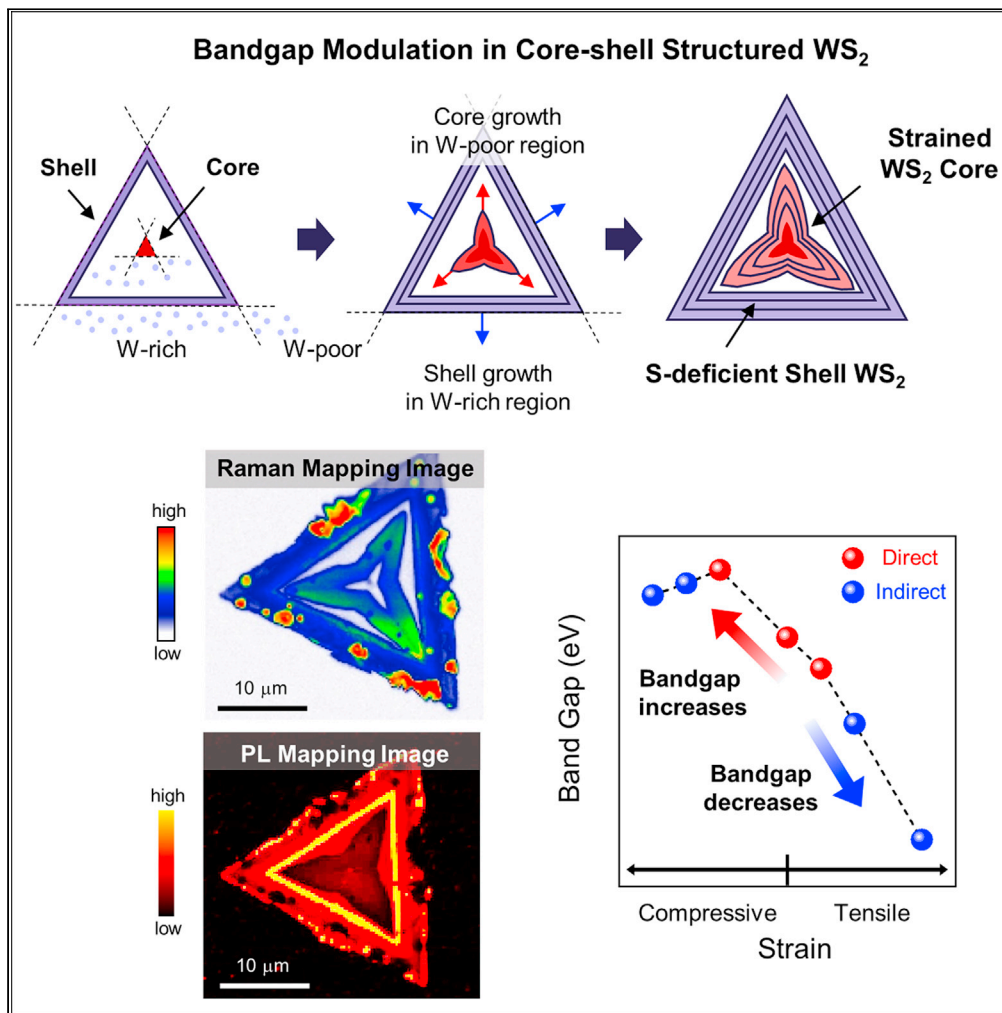


Article

Bandgap modulation in the two-dimensional core-shell-structured monolayers of WS₂

Seohui Kang,
Yonas Assefa
Eshete, Sujin Lee,
..., Sangheon Lee,
Suyeon Cho,
Heejun Yang

s.cho@ewha.ac.kr (S.C.)
h.yang@kaist.ac.kr (H.Y.)

Highlights
Core-shell-structured WS₂ monolayers with modulated bandgap are grown by CVD

Doping and strain effect in band structure are revealed by Raman and PL spectroscopy

Through DFT calculation, we showed that the bandgap can be tuned by the strain

Core-shell-structured WS₂ with different bandgap provides option to tune the bandgap

Kang et al., iScience 25, 103563
January 21, 2022 © 2021 The Author(s).
<https://doi.org/10.1016/j.isci.2021.103563>



Article

Bandgap modulation in the two-dimensional core-shell-structured monolayers of WS₂

Seohui Kang,¹ Yonas Assefa Eshete,² Sujin Lee,¹ Dongyeun Won,² Saemi Im,¹ Sangheon Lee,¹ Suyeon Cho,^{1,*} and Heejun Yang^{3,4,*}

SUMMARY

Tungsten disulfide (WS₂) has tunable bandgaps, which are required for diverse optoelectronic device applications. Here, we report the bandgap modulation in WS₂ monolayers with two-dimensional core-shell structures formed by unique growth mode in chemical vapor deposition (CVD). The core-shell structures in our CVD-grown WS₂ monolayers exhibit contrasts in optical images, Raman, and photoluminescence spectroscopy. The strain and doping effects in the WS₂, introduced by two different growth processes, generate PL peaks at 1.83 eV (at the core domain) and 1.98 eV (at the shell domain), which is distinct from conventional WS₂ with a primary PL peak at 2.02 eV. Our density functional theory (DFT) calculations explain the modulation of the optical bandgap in our core-shell-structured WS₂ monolayers by the strain, accompanying a direct-to-indirect bandgap transition. Thus, the core-shell-structured WS₂ monolayers provide a practical method to fabricate lateral heterostructures with different optical bandgaps, which are required for optoelectronic applications.

INTRODUCTION

Two-dimensional (2D) atomic crystals, such as graphene, hexagonal boron nitride (*h*-BN), and transition metal dichalcogenides (TMDs), have recently received considerable attention because of their unique 2D characteristics in physics and chemistry, which are promising for future optoelectronic devices (Radi-savljevic et al., 2011; Wang et al., 2012; Lopez-Sanchez et al., 2013; Jariwala et al., 2014). Among the various 2D atomic crystals, group 6 TMDs are considered as attractive semiconducting materials owing to their tunable bandgaps and layer-dependent exciton dynamics (Chhowalla et al., 2013; Ding et al., 2011). Hexagonal tungsten disulfide (2H-WS₂) is a semiconductor in group 6 TMDs, where its layers are weakly bonded by van der Waals interactions (Chhowalla et al., 2013; Butler et al., 2013). The 2H-WS₂ exhibits an indirect bandgap in its bulk and undergoes an indirect-to-direct bandgap transition as it is thinned down to a monolayer (Gutiérrez et al., 2013; Yun et al., 2012). The electronic band structures of WS₂ critically depend on the condition of the sample synthesis; thus, rigorous studies of the WS₂ grown by various processes are required.

Confocal PL and Raman spectroscopy are suitable techniques for characterizing 2D layered materials. Monolayer WS₂ has strong and distinct PL and Raman spectra owing to its direct bandgap. The uniform PL signal in a WS₂ flake indicates its highly crystalline structure (Gutiérrez et al., 2013; Cong et al., 2014; Peimyoo et al., 2013), which is preferred for transistor applications. Nevertheless, WS₂ monolayers grown by CVD exhibit various PL signals determined by the synthetic conditions; for example, it was reported that PL spectra were abnormally enhanced by abundant adsorbents that were formed during CVD growth (Peimyoo et al., 2013; Guterrez et al., 2013; Liu et al., 2016a; Jeong et al., 2017; Sheng et al., 2017; Hu et al., 2019).

The role of strain to modify electronic structures of 2D TMDs have been intensively studied by confocal PL and Raman spectroscopy (Conley et al., 2013; He et al., 2013; Zhu et al., 2013). When a tensile or compressive strain is applied on TMDs by using a stretchable or bendable substrate, the bandgap of the TMDs significantly changes and direct-to-indirect bandgap transition has been reported (Wang et al., 2015; He et al., 2016). In previous studies on CVD-grown WS₂, distinct intrinsic strains were introduced under different growth conditions; this was because of the different thermal expansion coefficients between the WS₂ and substrates (Feng et al., 2017; Shi et al., 2019). The theoretical calculations have also predicted that strain modifies the valence band maximum (VBM) and conduction band minimum (CBM) of

¹Department of Chemical Engineering and Materials Science, Graduate Program in System Health Science and Engineering, Ewha Womans University, Seoul 03760, Republic of Korea

²Department of Energy Science, Sungkyunkwan University, Suwon 16419, Republic of Korea

³Department of Physics, Korea Advanced Institute of Science and Technology (KAIST), Daejeon 34141, Republic of Korea

⁴Lead contact

*Correspondence:
s.cho@ewha.ac.kr (S.C.),
h.yang@kaist.ac.kr (H.Y.)

<https://doi.org/10.1016/j.isci.2021.103563>



semiconducting TMDs such as 2H-WS₂, which results in direct-indirect band gap transition (Yun et al., 2012; Wang et al., 2015; Shi et al., 2013; Chang et al., 2013; Desai et al., 2014; Johari and Shenoy, 2012; Peelaers and Van de Walle, 2012; Lu et al., 2012; Zhang et al., 2013; Maniadaki et al., 2016; Muoi et al., 2019). Accordingly, the growth mechanism in CVD remains to be further explored to understand and modulate the strain effects on the electronic properties of few-layered WS₂.

Recently, heterogeneous 2D TMDs grown by CVD have been reported with various geometries (Jeong et al., 2017; Chen et al., 2014; Wang et al., 2018; Shinde et al., 2018). Jeong et al. reported WS₂ with a hexagonal geometry that is segmented into alternating triangle domains: S-deficient and W-deficient domains (Jeong et al., 2017). The heterostructures with core metal oxides and shell TMDs have been found in a fullerene-like shape (Cain et al., 2016). Such TMDs show the multiple domains of the core and shell where nucleation- and diffusion-dominated growth processes coexist (Withanage et al., 2020). The core-shell structure growth by CVD offers a unique technique for engineering electronic heterostructures for diverse optoelectronic applications with TMDs (Fang et al., 2020; Jo et al., 2019).

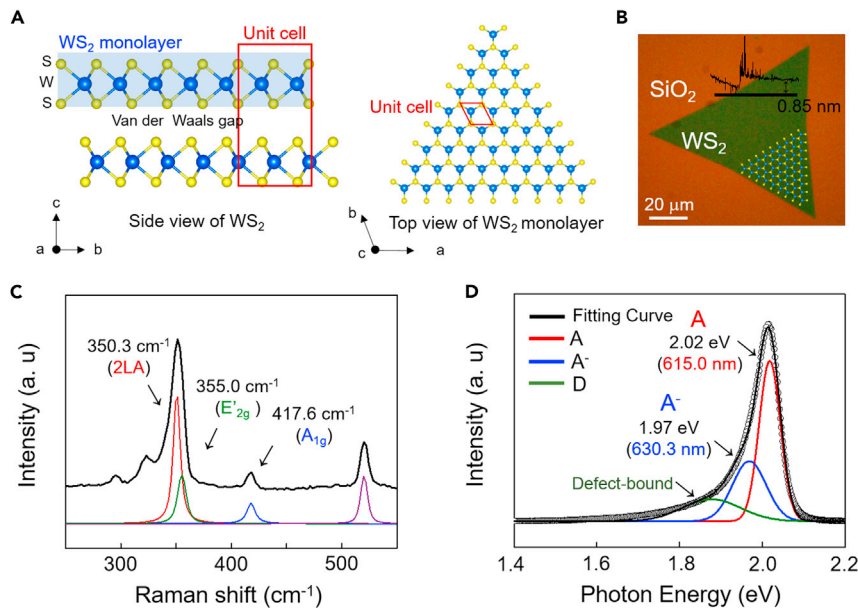
In this study, we conducted thorough PL and Raman spectroscopy on core-shell-structured WS₂ monolayers grown by CVD. The core-shell-structured WS₂ monolayer possessed multiple domains that were optically distinguished as a core and surrounding-shell domain. Our WS₂ monolayers with core-shell structures showed the prominent Raman modes of conventional WS₂, 2LA, E'₂g, and A₁g. However, in contrast to conventional WS₂ monolayers with PL peaks at 2.02 eV, the core-shell-structured WS₂ exhibited weakened PL peaks located at 1.83 eV and 1.98 eV in the core and shell WS₂, respectively. DFT calculations demonstrated that the lateral strain in the WS₂ monolayer, originating from its unique 2D geometrical growth, generated the practical modulation of the optical bandgap observed in the core and shell domains. Our study suggests that the subtle modulation of the optical bandgap can be realized by introducing strains in the CVD process, which provides unique lateral heterostructures for future optoelectronic devices. Lateral heterostructures with different bandgaps will realize a simple design of multi-functional optoelectronic devices, which is distinguished from previous studies on WO₃/WS₂ devices. For that purpose, our WS₂ monolayers grown by the 2D core-shell growth mode generate proper vacancies and strains in the 2D lattice, which is a novel engineering approach for future device applications, such as LED, photodetectors, and bipolar junction transistors (Kang et al., 2013; Pospischil et al., 2014; Baugher et al., 2014; Ross et al., 2014; Gong et al., 2013; Kim et al., 2021).

RESULTS AND DISCUSSION

As shown in Figure 1A, a three-atom-thick WS₂ monolayer consists of a W atomic layer sandwiched between top and bottom S atomic layers. Semiconducting WS₂ is referred to as 2H-WS₂ because two WS₂ atomic layers form a hexagonal unit cell. As shown in the top view of the WS₂ monolayer, the W and S atoms were arranged by a triangular lattice structure, showing the hexagonal symmetry of WS₂. The as-grown WS₂ monolayer possessed a triangle shape with a thickness of 0.85 nm, as shown in the optical image and AFM height profile in Figure 1B. Raman and PL spectroscopy confirmed that the WS₂ monolayer possessed a single domain owing to its uniform signals. As shown in Figure 1C, the single-domain WS₂ monolayer shows three main Raman peaks at 350.3 cm⁻¹, 355.0 cm⁻¹, and 417.6 cm⁻¹, which is consistent with the reported Raman active modes of WS₂; the three peaks correspond to the 2LA (second-order longitudinal acoustic Raman mode at point M), E'₂g, and A₁g of WS₂, respectively (Berkdemir et al., 2013).

The PL spectrum of single-domain WS₂ monolayer was fitted by three Gaussian curves: exciton emission (red curves, marked by "A"), negative trion emission (blue curves, marked by "A⁻"), and defect-bound exciton emission (green curves, marked by "D"). The PL spectrum showed a strong exciton emission at 615.0 nm with a low full-width half-maximum (FWHM) of 19.1 cm⁻¹, which corresponded to the previously reported exciton emission at 2.01–2.02 eV (Plechinger et al., 2015; Bellus et al., 2015; Zhu et al., 2015; Peimyoo et al., 2014). The small and broadened PL peak at approximately 630.3 nm with a high FWHM of 50.6 cm⁻¹ can be attributed to the electron-doped negative trion peak of WS₂ (Zhu et al., 2015; Peimyoo et al., 2014). The detailed Gaussian fittings for the Raman and PL spectra are summarized in the supporting materials (see Tables S1 and S2).

Although most CVD-grown WS₂ samples have a single domain with a uniform thickness and optical contrast, as shown in Figure 1, multi-domain WS₂ flakes are also found with a non-uniform optical contrast, as shown in Figure 2A. Both single- and multi-domain WS₂ flakes were simultaneously grown on a substrate

**Figure 1. Single-domain WS₂ grown by chemical vapor deposition**

(A) Crystal structure of hexagonal WS₂. Side view of the WS₂ and top view of the WS₂ monolayer with a unit cell (red rectangles).

(B) Optical image of the WS₂ monolayer with a profile of thickness, which is estimated as 0.85 nm by AFM measurement.

(C and D) (C) Raman and (D) PL spectra of single-domain WS₂ with fitted curves. In the PL spectra, the red, blue, and green fitting curves labeled with A, A⁻, and D represent emission of exciton, trion, and defect-bound exciton, respectively.

(see Figure S1 for more information). Although we continuously supply S source during the CVD growth, local variation of W and S sources leads to the formation of single- and multi-domain WS₂ flakes. Optical microscopy showed that the interior core domain possessed a three-leg-starfish shape, and the surrounding shell domain possessed a triangular shape. Using AFM, we examined the thickness of the core-shell-structured WS₂ and its change across the border between the core and shell domains. The WS₂ flake with multiple domains was a monolayer with a thickness of 0.85 nm, as shown in the height profiles (line 1 in Figure 2B), without any change in the thickness across the border (line 2 in Figure 2B). The concentrations of W and S elements in the multi-domain WS₂ were measured by using electron probe microscope analysis (EPMA). Although the elemental analysis was challenging with the sub-nanometer thickness of multi-domain WS₂ monolayer (see Figure S2 in the supporting materials), we could observe the relative distribution of S as shown in Figure 2C; the core region has a little bit higher S concentration than the shell region, whereas the concentration of S is uniform within the domain except multilayer regions that are located at the shell boundary. The EPMA results demonstrate that the shell region has more S defects than the core region in our multi-domain WS₂ monolayers.

It has been reported that core-shell-structured MoS₂ monolayers can be synthesized by CVD with a similar geometry, as shown in Figure 2D (Zhang et al., 2017). According to the study, the growth of the core part of the WS₂ is stimulated at the corner of its nucleus (depicted as a red triangle in Figure 2D), whereas the growth of the shell part begins from W-rich edges (depicted as a violet triangle shell in Figure 2D). The two different growth modes for the core and shell domains proceeded separately in W-poor and W-rich regions, generating core and shell structures with boundaries, as shown in the schematic of Figure 2D. We found that the ratio of W to S in the shell domain is relatively higher than the core domain, which indicates that our multi-domain WS₂ monolayers have S-deficient shell domains. The core and shell domains are independently grown in our CVD growth via the 2D core-shell growth mode.

The core-shell-structured WS₂ monolayer was characterized by confocal Raman mapping with a step size of 250 nm. The entire area of the core-shell-structured WS₂ monolayer showed the consistent Raman active modes of WS₂, corresponding to the 2LA, E'_{2g}, and A_{1g} modes of WS₂. Figure 3A shows two Raman mapping images of a core-shell-structured WS₂ monolayer (marked with a white circle in Figure 2A) with the

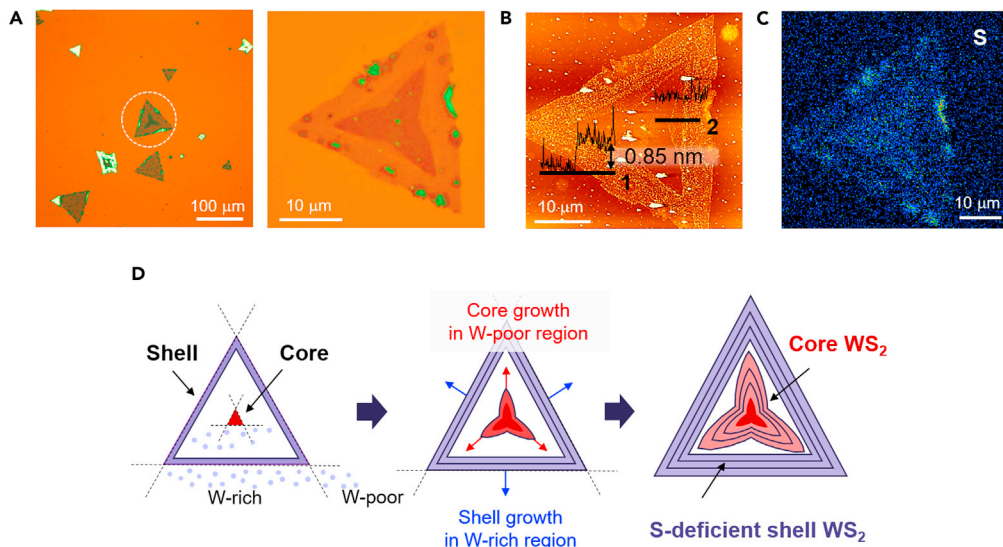


Figure 2. WS₂ with multi-domains grown by core-shell growth mode

(A) Optical images of the WS₂ flakes with a triangular shape on a SiO₂/Si substrate. A multi-domain WS₂ flake is marked with a dashed white circle (left panel), and its magnified image is shown in the right panel.

(B) AFM image of the multi-domain WS₂ monolayer flake. Height profiles across the border of WS₂ (line 1) and the different optical contrast region inside the WS₂ flake (line 2) are shown in the AFM image.

(C) EPMA mapping image of S in the core-shell WS₂ monolayer.

(D) Schematic images for core-shell growth mechanism for multi-domains WS₂.

peaks of 2LA and A_{1g}. Based on the optical microscopy and Raman spectroscopy results, in this study, we divided the core-shell-structured WS₂ monolayer into four regions: (1) shell, (2) shell boundary, (3) core boundary, and (4) core. The four regions are marked by letters from "a" to "d" in the inset of Figure 3B. We selected four points to represent each region whose Raman intensity and shift mapping are shown in Figure 3B and Figure S3, respectively. The Raman spectra from the four regions were analyzed by fitting them with Gaussian curves; the resulting fitting parameters are summarized in Table S1.

The region marked by "a" in the inset of Figure 3B, a WS₂ shell domain, has Raman peaks at 347.6 cm⁻¹, 355.0 cm⁻¹, and 416.6 cm⁻¹, which can be assigned to the Raman active modes of 2LA, E'_{2g} and A_{1g} in the conventional WS₂. Compared with the WS₂ monolayer with a single domain, the shell domain of the core-shell-structured WS₂ monolayer exhibited a red-shifted A_{1g} mode by 1.0 cm⁻¹ without any change in the E'_{2g} mode. Considering that the E'_{2g} and A_{1g} modes are sensitive to the strain and doping effect (Peimyoo et al., 2014; Wang et al., 2015; Conley et al., 2013; Zhu et al., 2013; Chakraborty et al., 2012; Nan et al., 2014), respectively, the red-shifted A_{1g} peak in the shell domain indicated effective n-type doping, probably due to sulfur deficiency. However, no significant strain effect was observed in the sample.

In the core domain of WS₂, marked with the position d in the inset of Figure 3B, the Raman peaks exhibit red-shifted E'_{2g} and A_{1g} peaks by 1.3 cm⁻¹ and 1.2 cm⁻¹, respectively. In contrast to the unchanged E'_{2g} peak in the shell domain, the core domain exhibited a red-shifted E'_{2g} peak, which can be ascribed to the strain effect, particularly by tensile strain (Peimyoo et al., 2014; Wang et al., 2015; Conley et al., 2013; Zhu et al., 2013). The doping effect in the core domain was comparable with that in the shell domain because of the similar red-shifted A_{1g} Raman peak in the core and shell domains. The Raman features of our core-shell-structured WS₂ monolayer are different from those of multi-domain hexagonal WS₂ with a large blue-shifted A_{1g}, which was explained by the polarity (p)-doping effect in the W-deficient domain (Jeong et al., 2017). Therefore, we interpret our results using the different p-doping and strain effects; the S-deficient shell domain possessed an n-type doping effect, whereas the core domain experienced a tensile strain together with an n-type doping effect.

Considering that defects could decompose TMDs (Fang et al., 2019; Gao et al., 2016), we confirmed the stability of our multi-domain WS₂ monolayer. The confocal Raman and PL and optical microscope images

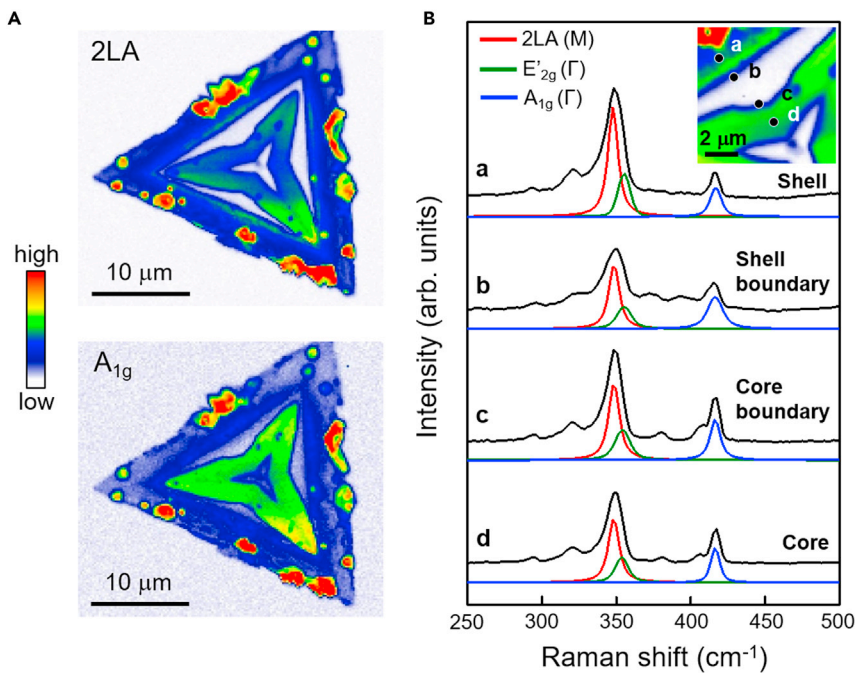


Figure 3. Raman mapping and spectra of core-shell-structured WS₂

(A) Raman intensity mapping with two Raman active modes, 2LA (350.3 cm⁻¹) and A_{1g} (417.6 cm⁻¹), of WS₂.
(B) Raman spectra with fitted curves at the locations of a, b, c, and d in the inset of the Raman intensity mapping image. The Raman were fitted by multiple Gaussian curves, and the detailed fitting parameters are described in Table S1 in supporting materials.

of a same multi-domain WS₂ flake in Figure S4 show that the sample is stable over two years without significant decomposition. It has been reported that most chalcogen vacancies (S deficiencies or defects) are passivated by oxygen atoms (Bui et al., 2015; Liu et al., 2016b). For example, Cui et al. recently reported that strong W-O bonds are responsible for the superior environment stability of WS₂ by incorporating O atoms at the S vacancy sites of WS₂ (Cui et al., 2021).

Confocal PL spectroscopy revealed that the PL spectra of the core-shell-structured WS₂ monolayer significantly varied at different locations in the flake, which is in contrast to a single-domain WS₂ monolayer. As shown in Figure 4A, PL intensity mapping images show a large variation of PL signals between two exciton energies of 1.98 eV (at the shell region) and 1.83 eV (at the core region). Notably, the core and shell domains of the WS₂ monolayer exhibited 5–10 times weaker PL emission than the boundary regions (see Figure S5). The line profiles of the PL mapping image shown in Figure 4B demonstrate that the PL intensity and exciton photon energy significantly change across the line profile in the core-shell-structured WS₂ monolayer. The quenched PL spectra in the S-deficient shell domain can be explained by nonradiative carrier decay in defect-related states, which have been reported as deep trap sites in defective TMDs (Jeong et al., 2017; Liu et al., 2016a; Su et al., 2016). For the strain effect in the core domain of our core-shell-structured WS₂ monolayer, the dramatically quenched PL spectrum centered at 1.83 eV can be explained by direct-to-indirect bandgap transitions, as often observed in strained TMDs (Wang et al., 2015; Conley et al., 2013; Lu et al., 2012; Kumar and Ahluwalia, 2013).

The boundaries between the core and shell regions in our WS₂ flakes produced stronger PL spectra than the core and shell regions. The PL spectra were deconvoluted into two emissions, as shown in Figure 4C. The enhanced PL intensities at the boundaries can be explained by the chemical doping, oxidation, and chemisorption that occurred at the boundary region. Notably, several TMDs exhibited increased PL spectra with similar origins (Gutiérrez et al., 2013; Nan et al., 2014; Tongay et al., 2013; Sheng et al., 2017). The PL signals of the shell and core boundary comprised two sets of peaks (A and A⁻ peaks), as shown in Figure 4C. The energy difference of 0.043 eV for excitons and trions was reported in previous

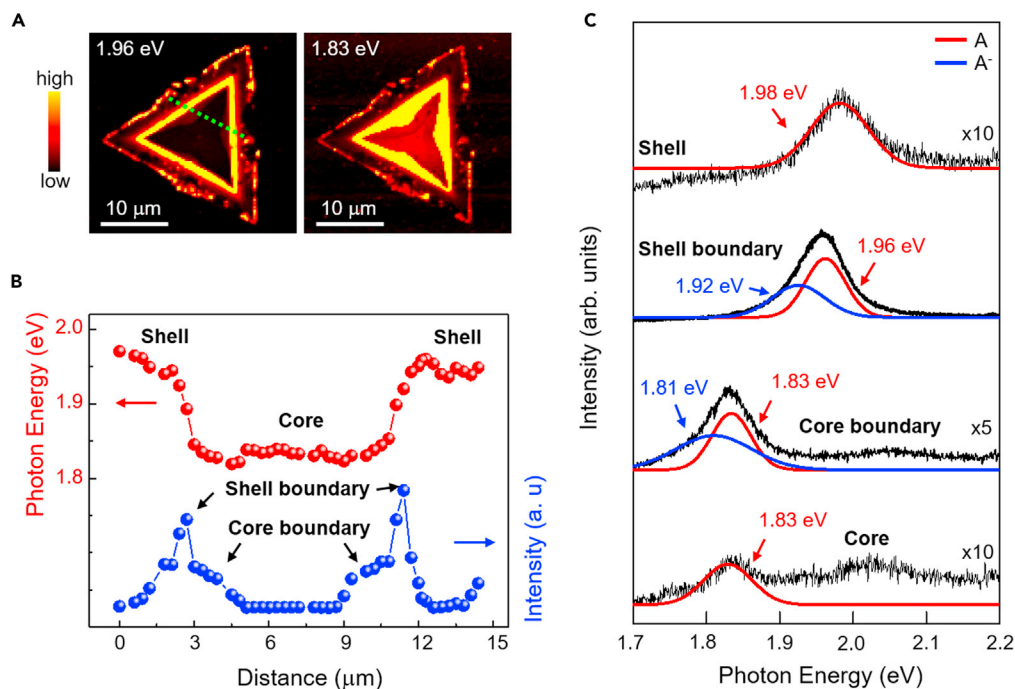


Figure 4. Photoluminescence study of core-shell-structured WS_2

- (A) PL intensity mapping with two photon energies, 1.96 eV and 1.83 eV.
- (B) Line profiles of the PL mapping image with exciton photon energy and PL intensity across the sample, collected along the dashed green line of Figure 4A.
- (C) PL spectra with fitted curves at the core and shell with PL spectra at the boundaries of the core and shell. The PL spectra were fitted by multiple Gaussian curves, and the detailed fitting parameters are described in Table S2 in the supporting materials.

studies (Pleckinger et al., 2015); thus, the two peaks (A and A^- peaks) in our PL spectra are attributed to the generation of excitons and trions in WS_2 .

Zhang et al. reported core-shell-structured MoS_2 monolayers synthesized by CVD using a solid precursor of metal oxide (Zhang et al., 2017). In this study, the metal oxide precursor and S source provided a sufficient quantity of Mo and S in the growth process. Therefore, the core and shell domains were grown with a uniform chemical composition and merged into a flake with a boundary that was optically hidden but distinguished by PL spectroscopy. The enhanced PL intensity resulted from the p-doping and strain effects at the (optically) hidden boundary. Our core-shell-structured WS_2 was synthesized under different conditions using a precoated hydrate W source on the substrate. Thus, a limited amount of W was supplied, and the WS_2 monolayers could not merge their domains and boundaries having different chemical compositions.

Compression or tensile strains were found in many TMDs, mostly due to the formation of defects and dislocations during the CVD growth of the 2D geometry (Feng et al., 2017; Shi et al., 2019; Liu et al., 2014; Kataria et al., 2017). Previous studies have shown that the strains undergo direct-to-indirect bandgap transitions and changes in the emitted photon energy in the PL spectra of the TMDs (Yun et al., 2012; Wang et al., 2015; Shi et al., 2013; He et al., 2016; Chang et al., 2013; Desai et al., 2014). We conducted DFT calculations to show that the electronic structure of the WS_2 monolayer could be modulated by the lateral strains. As shown in Figure 5A, a pristine WS_2 monolayer without strain ($\epsilon = 0\%$) has a valence band maximum (VBM) and conduction band minimum (CBM) at the K point, indicating a direct bandgap semiconductor with a calculated bandgap of 1.83 eV. When a lateral strain (ϵ) was applied to the WS_2 monolayer by changing the lattice constant a to ea in the range from 0% to $\pm 2.0\%$ (positive ϵ for a tensile strain and negative ϵ for a compressive strain), the electronic structure of the WS_2 changed. The VBM and CBM occurred at different symmetry points: KL, AL, and ΓH , depending on the strength of the strain (Figure 5B).

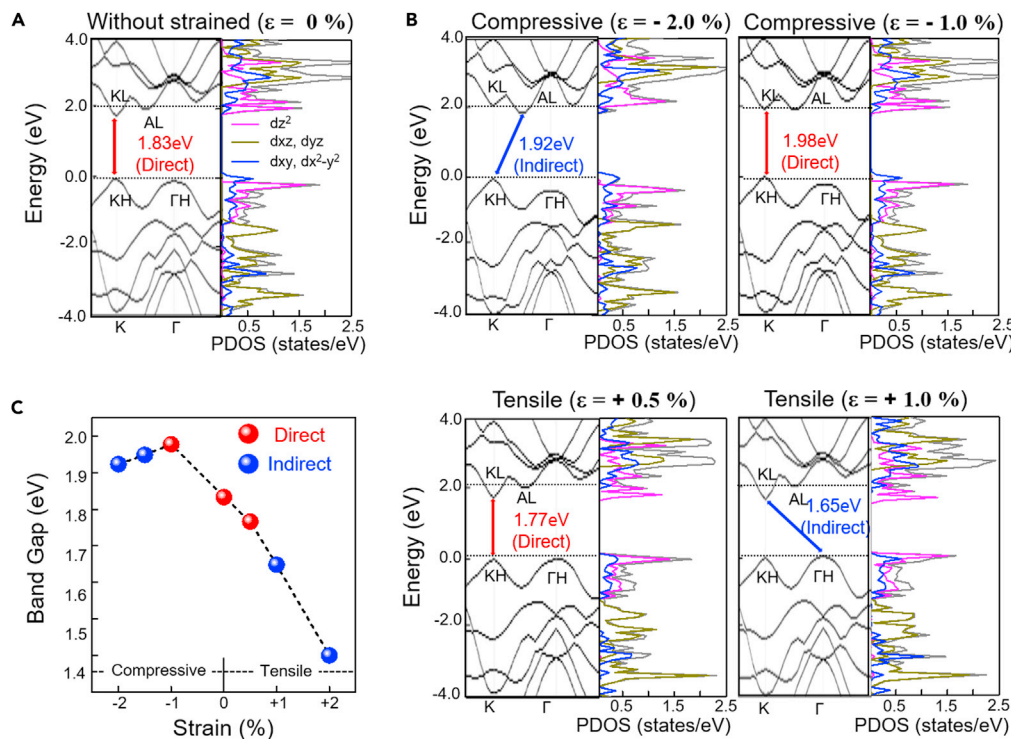


Figure 5. The calculated band structure and corresponding PDOS of monolayer WS₂ under strain

(A and B) (A) $\varepsilon = 0\%$ (unstrained), (B) $\varepsilon = -1.0\%$, -2.0% , $+0.5\%$, and $+1.0\%$.

(C) Calculated band gap of the strained WS₂ monolayer as a function of strain.

The bandgaps of the WS₂ monolayer in the presence of strain, as estimated by DFT calculations, are summarized in Figure 5C. The bandgap of the WS₂ monolayer increased in the range of $-2\% \leq \varepsilon \leq -1\%$, and thereafter, it decreased in the range of $+0.5\% \leq \varepsilon \leq +2\%$. Thus, the largest direct bandgap (1.98 eV) was obtained with a strain of -1.0% , where the bandgap of the WS₂ monolayer decreased with strain accompanying the direct-to-indirect bandgap transition. Our DFT calculations exhibit strain-induced bandgap changes that are consistent with previous works. For example, it has been reported that the bandgap of WS₂ monolayer decreases by a tensile strain, and strain-induced direct-to-indirect bandgap transition occurs as the tensile strain reaches 2.6% (Wang et al., 2015; He et al., 2016). In our DFT calculations, the decrease of bandgap and its transition from direct-to-indirect bandgap are similarly observed in Figure 5C. As for compressive strain (i.e., negative strain in Figure 5C), direct-to-indirect bandgap transition is observed at a strain of -1.5% , which is similar to previous reports with MoS₂ (Chang et al., 2013; Yun et al., 2012; Muoi et al., 2019). The bandgap changes and its direct-to-indirect transition could be explained by strain-induced modification of the coupling strength between atomic orbitals in TMDs. Accordingly, we demonstrate the orbital nature of electronic band structures of WS₂, such as d_{z2}, d_{xy}, and d_{x2-y2}, in Figure 5. The direct-to-indirect bandgap transition with such decreased bandgaps explains our experimental findings in the Raman and PL spectroscopy: our core-shell-structured WS₂ monolayer was under strain, resulting in the lateral modulation of the bandgap (Wang et al., 2015; Conley et al., 2013; Lu et al., 2012; Kumar and Ahluwalia, 2013).

Conclusion

We investigated WS₂ monolayers grown by CVD. Certain flakes exhibited a multi-domain structure, which was similar to the previously reported core-shell structure of MoS₂. However, the control of the quantity of W allowed for a novel type of core-shell structure in the WS₂. The core-shell growth mode in our CVD provided a lateral electronic heterostructure to modulate the bandgap of WS₂ in a geometry with two domains: a core and an S-deficient shell. The two domains showed distinct Raman and PL spectra. The core-shell-structured WS₂ monolayer exhibited PL spectra with a variation of optical bandgap at approximately 9.4% with a broad, weak, and blue-shifted PL peak. Our DFT calculations showed that the optical bandgap of the WS₂ monolayer can be decreased by tensile strain on the core domain of the WS₂ monolayer using a direct-to-indirect bandgap transition.

Limitations of the study

In our study, the core and shell domains in WS_2 monolayers have distinct bandgaps, resulting in optically distinguishable images of the core and shell domains in WS_2 monolayers. Therefore, we observed core-shell structures in WS_2 by optical microscope, and around 4 out of 10 flakes have such clear core-shell structures. We have tried to synthesize WS_2 monolayers uniformly with the core-shell structures. But the subtle CVD conditions make it hard to uniformly control the growth mode that requires locally insufficient supply of W and S sources. Therefore, further study to control the growth mode is required for homogeneous WS_2 flakes with core-shell structures.

STAR METHODS

Detailed methods are provided in the online version of this paper and include the following:

- KEY RESOURCES TABLE
- RESOURCE AVAILABILITY
 - Lead contact
 - Materials availability
 - Data and code availability
- EXPERIMENTAL MODEL AND SUBJECT DETAILS
- METHOD DETAILS
 - Sample synthesis
 - Sample characterization
 - Computational method
- QUANTIFICATION AND STATISTICAL ANALYSIS

SUPPLEMENTAL INFORMATION

Supplemental information can be found online at <https://doi.org/10.1016/j.isci.2021.103563>.

ACKNOWLEDGMENTS

This work was supported by the Basic Science Research Program through the National Research Foundation of Korea (NRF) funded by the Ministry of Science, ICT and Future Planning (2020R1A2C2003377). H.Y. acknowledges support from the National Research Foundation of Korea (NRF) under Grant No. NRF-2020R1A2B5B02002548.

AUTHOR CONTRIBUTIONS

Conceptualization, S. K., S. C., and H. Y.; Investigation & Resources, S. K., Y. A. E., Sujin Lee, and D. W.; Validation & Data Curation, S. I. and Sangheon Lee; Writing—Original Draft, S. K.; Writing—Review & Editing, Supervision, S. C. and H. Y.

DECLARATION OF INTERESTS

The authors declare no competing financial interests.

Received: August 5, 2021

Revised: November 15, 2021

Accepted: December 1, 2021

Published: January 21, 2022

REFERENCES

- Baugher, B.W., Churchill, H.O., Yang, Y., and Jarillo-Herrero, P. (2014). Optoelectronic devices based on electrically tunable p–n diodes in a monolayer dichalcogenide. *Nat. Nanotechnol.* 9, 262–267.
- Bellus, M.Z., Ceballos, F., Chiu, H.-Y., and Zhao, H. (2015). Tightly bound trions in transition metal dichalcogenide heterostructures. *ACS Nano* 9, 6459–6464.
- Berkdemir, A., Gutiérrez, H.R., Botello-Méndez, A.R., Pereira-López, N., Elías, A.L., Chia, C.-I., Wang, B., Crespi, V.H., López-Urías, F., Charlier, J.-C., et al. (2013). Identification of individual and few layers of WS_2 using Raman spectroscopy. *Sci. Rep.* 3, 1–8.
- Bui, V.Q., Pham, T.-T., Le, D.A., Thi, C.M., and Le, H.M. (2015). A first-principles investigation of various gas (CO , H_2O , NO , and O_2) absorptions on a WS_2 monolayer: stability and electronic properties. *J. Condens. Matter Phys.* 27, 305005.
- Butler, S.Z., Hollen, S.M., Cao, L., Cui, Y., Gupta, J.A., Gutiérrez, H.R., Heinz, T.F., Hong, S.S., Huang, J., Ismach, A.F., et al. (2013). Progress, challenges, and opportunities in two-dimensional materials beyond graphene. *ACS Nano* 7, 2898–2926.

Plechinger, G., Nagler, P., Kraus, J., Paradiso, N., Strunk, C., Schüller, C., and Korn, T. (2015). Identification of excitons, trions and biexcitons in single-layer WS₂. *Phys. Status Solidi RRL* 9, 457–461.

Pospischil, A., Furchi, M.M., and Mueller, T. (2014). Solar-energy conversion and light emission in an atomic monolayer p–n diode. *Nat. Nanotechnol.* 9, 257–261.

Radisavljevic, B., Radenovic, A., Brivio, J., Giacometti, V., and Kis, A. (2011). Single-layer MoS₂ transistors. *Nat. Nanotechnol.* 6, 147–150.

Ross, J.S., Klement, P., Jones, A.M., Ghimire, N.J., Yan, J., Mandrus, D.G., Taniguchi, T., Watanabe, K., Kitamura, K., Wang, Y., et al. (2014). Electrically tunable excitonic light-emitting diodes based on monolayer WS₂ p–n junctions. *Nat. Nanotechnol.* 9, 268–272.

Sheng, Y., Wang, X., Fujisawa, K., Ying, S., Elias, A.L., Lin, Z., Xu, W., Zhou, Y., Korsunsky, A.M., Bhaskaran, H., et al. (2017). Photoluminescence segmentation within individual hexagonal monolayer tungsten disulfide domains grown by chemical vapor deposition. *ACS Appl. Mater. Interface* 9, 15005–15014.

Shi, H., Pan, H., Zhang, Y.-W., and Yakobson, B.I. (2013). Quasiparticle band structures and optical properties of strained monolayer MoS₂ and WS₂. *Phys. Rev. B* 87, 155304.

Shi, B., Zhou, D., Fang, S., Djebbi, K., Feng, S., Zhao, H., Tlili, C., and Wang, D. (2019). Facile and controllable synthesis of large-area monolayer WS₂ flakes based on WO₃ precursor drop-casted

substrates by chemical vapor deposition. *Nanomaterials* 9, 578.

Shinde, S.M., Dhakal, K.P., Chen, X., Yun, W.S., Lee, J., Kim, H., and Ahn, J.-H. (2018). Stacking-controllable interlayer coupling and symmetric configuration of multilayered MoS₂. *NPG Asia Mater.* 10, e468.

Su, W., Jin, L., Qu, X., Huo, D., and Yang, L. (2016). Defect passivation induced strong photoluminescence enhancement of rhombic monolayer MoS₂. *Phys. Chem. Chem. Phys.* 18, 14001–14006.

Tongay, S., Suh, J., Ataca, C., Fan, W., Luce, A., Kang, J.S., Liu, J., Ko, C., Raghunathanan, R., Zhou, J., et al. (2013). Defects activated photoluminescence in two-dimensional semiconductors: interplay between bound, charged and free excitons. *Sci. Rep.* 3, 1–5.

Wang, Q.H., Kalantar-Zadeh, K., Kis, A., Coleman, J.N., and Strano, M.S. (2012). Electronics and optoelectronics of two-dimensional transition metal dichalcogenides. *Nat. Nanotechnol.* 7, 699–712.

Wang, Y., Cong, C., Yang, W., Shang, J., Peimyoo, N., Chen, Y., Kang, J., Wang, J., Huang, W., and Yu, T. (2015). Strain-induced direct–indirect bandgap transition and phonon modulation in monolayer WS₂. *Nano Res.* 8, 2562–2572.

Wang, J., Cai, X., Shi, R., Wu, Z., Wang, W., Long, G., Tang, Y., Cai, N., Ouyang, W., Geng, P., et al. (2018). Twin defect derived growth of atomically thin MoS₂ dendrites. *ACS Nano* 12, 635–643.

Withanage, S.S., Charles, V., Chamlagain, B., Wheeler, R., Mou, S., and Khondaker, S.I. (2020). Synthesis of highly dense MoO₃/MoS₂ core–shell nanoparticles via chemical vapor deposition. *Nanotechnology* 32, 055605.

Yun, W.S., Han, S., Hong, S.C., Kim, I.G., and Lee, J. (2012). Thickness and strain effects on electronic structures of transition metal dichalcogenides: 2H-MX₂ semiconductors (M=Mo, W; X= S, Se, Te). *Phys. Rev. B* 85, 033305.

Yun, S.J., Chae, S.H., Kim, H., Park, J.C., Park, J.H., Han, G.H., Lee, J.S., Kim, S.M., Oh, H.M., Seok, J., et al. (2015). Synthesis of centimeter-scale monolayer tungsten disulfide film on gold foils. *ACS Nano* 9, 5510–5519.

Zhang, Q., Cheng, Y., Gan, L.Y., and Schwingenschlögl, U. (2013). Giant valley drifts in uniaxially strained monolayer MoS₂. *Phys. Rev. B* 88, 245447.

Zhang, W., Lin, Y., Wang, Q., Li, W., Wang, Z., Song, J., Li, X., Zhang, L., Zhu, L., and Xu, X. (2017). Well-hidden grain boundary in the monolayer MoS₂ formed by a two-dimensional core–shell growth mode. *ACS Nano* 11, 10608–10615.

Zhu, C., Wang, G., Liu, B., Marie, X., Qiao, X., Zhang, X., Wu, X., Fan, H., Tan, P., Amand, T., and Urbaszek, B. (2013). Strain tuning of optical emission energy and polarization in monolayer and bilayer MoS₂. *Phys. Rev. B* 88, 121301.

Zhu, B., Chen, X., and Cui, X. (2015). Exciton binding energy of monolayer WS₂. *Sci. Rep.* 5, 1–5.

STAR★METHODS

KEY RESOURCES TABLE

REAGENT or RESOURCE	SOURCE	IDENTIFIER
Chemicals, Peptides, and Recombinant Proteins		
Ammonium metatungstate hydrate	Sigma-Aldrich	CAS: 12333-11-8
Sodium cholate hydrate	Sigma-Aldrich	CAS: 206986-87-0
OptiPrep™ Density Gradient Medium	Sigma-Aldrich	CAS: 92339-11-2
Sulfur powder	Sigma-Aldrich	CAS: 7704-34-9
Other		
Chemical Vapor Deposition	NanoTech Planet	http://www.ntplanet.co.kr/
Raman spectroscopy	Nanobase	https://www.nanobase.co.kr/
AFM	Hitachi	https://www.hitachi-hightech.com/global/science/products/microscopes/afm/
Software and algorithms		
OriginPro 9.0	OriginLab Corporation	https://www.originlab.com/
Vienna ab-initio Simulation Package (VASP)	Kresse and Furthmüller (1996)	https://www.vasp.at/

RESOURCE AVAILABILITY

Lead contact

Further information and requests for resource and reagents should be directed to and will be fulfilled by Lead Contact, Heejun Yang (h.yang@kaist.ac.kr).

Materials availability

All unique/stable reagents generated in this study are available from the Lead Contact with a completed Materials Transfer Agreement.

Data and code availability

Any additional information required to reanalyze the data reported in this paper is available from the lead contact upon request. No new code was generated during the course of this study.

EXPERIMENTAL MODEL AND SUBJECT DETAILS

Our study does not use experimental models typical in the life sciences.

METHOD DETAILS

Sample synthesis

WS₂ monolayers were grown by CVD on a SiO₂ (300 nm)/Si substrate. Ammonium metatungstate hydrate ((NH₄)₆H₂W₁₂O₄₀·xH₂O (Sigma-Aldrich, ≥ 66.5% (W)) was used as a W source and sodium cholate hydrate (Sigma-Aldrich) was used as a promoter, which were dissolved in DI water separately. Then, they were well-mixed with a medium solution (OptiPrep). After dropping the mixed solution onto the Si/SiO₂ substrate, we conducted spin-coating process to spread the solution uniformly (Jeong et al., 2017; Yun et al., 2015). S powder (Sigma Aldrich, ≥ 99.95 %) was supplied continuously during the CVD process. A two-zone furnace was separately heated with a steady flow of Ar gas, 500 standard cubic centimeters per minute (sccm), to the set temperatures with a ramping rate: 200°C at 33°C/min for the S source and 770°C with 128°C/min for the SiO₂/Si substrate with W. The temperature was maintained at the set temperature for 12 min, and afterward, the furnace was gradually cooled to room temperature.

Sample characterization

Atomic force microscopy (AFM) measurements were performed using a Hitachi AFM (5100N, Japan) in non-contact mode. Confocal Raman spectroscopy and PL spectroscopy were performed (XperRAM S series, Nanobase) with a wavelength of 532 nm for laser excitation. To avoid sample damage, we used an excitation laser power of less than 3 mW. All Raman peaks were calibrated using the Raman peak of Si located at 520 cm^{-1} .

Computational method

The geometry of the WS₂ structures with different strains was optimized using DFT as implemented in the Vienna ab-initio Simulation Package (VASP) ([Kresse and Furthmüller, 1996](#)) with projector augmented wave (PAW) pseudopotentials. All calculations were performed using the generalized gradient approximation (GGA) in the form of Perdew–Burke–Ernzerhof (PBE) ([Perdew et al., 1996](#)). We employed a cut-off energy for plane waves at 400 eV for all the calculations. All the atom positions were optimized until the convergence tolerance of the force was less than 0.001 eV/Å. A vacuum space of 10 Å in the z-direction was introduced to avoid interactions between adjacent periodic systems. The (24 × 24 × 1) Γ -centered Monkhorst–Pack meshes in the Brillouin zone ([Monkhorst and Pack, 1976](#)) were employed for optimization. Band structure calculations were performed along the high-symmetry path of M–K– Γ –M. The equilibrium lattice parameters of $a = 0.318\text{ nm}$, and $c = 1.311\text{ nm}$ were used to simulate the hexagonal (space group: P6₃/mmc) WS₂ monolayer. For the calculation of electronic structures modified by compression or tensile strain, we changed the lattice constants (a and b) with a portion from –2.0 to 2.0%, keeping the same volume with the small lattice constant changes.

QUANTIFICATION AND STATISTICAL ANALYSIS

Our study does not include statistical analysis or quantification.